



Shangtong Chen · Lei Guo · Yong Li · Jintao Liu ·
Qi Kang · Wen Li

Capillary-driven flows in eccentric annuli under microgravity

Received: 25 April 2022 / Accepted: 8 October 2022 / Published online: 15 November 2022
© The Author(s), under exclusive licence to Springer-Verlag GmbH Germany, part of Springer Nature 2022

Abstract The capillary-driven flow is an essential portion of liquid behavior under microgravity. Capillary-driven flows in eccentric annuli under microgravity are deeply analyzed in this paper. A second-order differential equation for the climbing height of liquid is derived. It can be solved with the Runge–Kutta method with appropriate initial conditions. The influences of the dynamic angle, the friction force on the annulus wall and the liquid meniscus in the reservoir on liquid behaviors are all considered in this paper. Moreover, effects of eccentricity on flow resistance and flow speed are discussed. This study has been verified by numerical simulation with the volume of fluid method.

Keywords Capillary-driven flow · Eccentric annulus · Volume of fluid method · Microgravity

1 Introduction

Abundant achievements have been made in the research of flow in concentric and eccentric annuli. For example, Snyder and Goldstein studied fully developed flows in eccentric annuli and proposed an exact solution for the velocity distribution [1]. The flow in the annulus has been proved to be useful as a mode for longitudinal flows in tube bundles. Satellite thrusters usually consist of concentric components to mix oxidizer and combustion. However, the problem of tube misalignment often happens. It is essential to master characteristics of capillary-driven flow in eccentric annuli under microgravity.

Since the substantial Lucas–Washburn equation was derived [2], capillary-driven flows in tubes and other kinds of containers have been widely studied. Levine et al. [3] derived the dynamic equation of capillary rise in cylindrical tubes and the convective loss at the tube entrance was considered for the first time. Stange et al. [4] presented a more comprehensive dynamic equation by considering the meniscus reorientation, the dynamic contact angle and the development of flows. Chen et al. [5] analyzed flows in oval tubes and proposed a new flow mode in which the entire flow can be divided into two regions. Capillary-driven flows in tubes with varying cross section [6–10], in complex containers [11] and in containers with axisymmetric geometries [12] were also deeply analyzed. The inverse problem of capillary imbibition [13], the oscillatory regime of capillary rise [14] and the effects of dynamic contact angle and initial liquid volume on capillary-driven flows [15, 16] were discussed in detail as well.

S. Chen · L. Guo · Y. Li · J. Liu · W. Li (✉)
Beijing Institute of Control Engineering, China Academy of Space Technology, Beijing 100094, China
e-mail: gradylee@126.com

Q. Kang
Institute of Mechanics, Chinese Academy of Sciences, Beijing 100190, China

Q. Kang
College of Engineering and Science, University of Chinese Academy of Sciences, Beijing 100049, China

The capillary-driven flow in corners has also attracted much attention. Weislogel and Lichter [17] proposed a dynamic model of the capillary flow in sharp inner corners (尖内角). It was further extended to interior corners with different wettability [18] and rounded interior corners [19]. Capillary flows in the interior corner formed by cylindrical and planar walls [20], in the narrow gap between two vertical plates making a small angle [21], in the curved interior corner [22], in the narrow and tilting corner [23], and in the small corner formed by two curved corners [24] were also explored in detail, and the dynamic equations of flows in these situations were presented.

The capillary rise behavior of liquid between parallel plates was studied by Dreyer et al. [25]. They divided the whole flow process into three regions. The lattice Boltzmann method based on field mediators was adopted by Wolf et al. [26] to simulate the capillary rise behavior between parallel plates. Liquid penetration through the metal wire mesh between parallel plates was analyzed by Weng et al. [27]. Klatte et al. [28] explored steady capillary-driven flows in open channels, and a fast numerical procedure was proposed. Equilibrium capillary surfaces [29, 30] and influences of the capillarity on a creeping film flow [31] were also explored. Theories of capillary-driven flows and numerical simulations were adopted to analyze liquid behaviors in propellant tanks under microgravity and optimize propellant management devices (PMD) [32–35].

However, capillary-driven flows in eccentric annuli have not been studied yet, and the influences of eccentricity on the capillary flow are still unknown. In this study, a theory for the capillary rise in eccentric annuli under microgravity is developed, and the effects of the dynamic contact angle, the pressure loss force at the entrance, the friction force and the curved liquid surface in the reservoir are all considered. The theory has been verified by numerical simulation based on the volume of fluid (VOF) method. Besides, the differential equation is transformed into a sum of forces acting on the control volume. Effects of different forces are discussed in detail, and the influences of eccentricity on the capillary flow are deeply analyzed.

2 Theoretical analysis

The vertical cross-sectional view of the theoretical model is shown in Fig. 1. The eccentric annulus is immersed into the liquid vertically from above with the immersion depth of h_0 . The radius of the curved free surface of the liquid inside the reservoir is R_r , which is calculated from the distance a between the wetting barriers and the distance b between the centerline of the free surface inside the reservoir and the centerline of the annulus. Figure 2 shows a horizontal cross-sectional view of the annulus. The inner and outer radii of the annulus are r_i and r_o , respectively. The distance between the centers of inner and outer tubes is e . The dynamic contact angles on the inner and outer walls are α_i and α_o , respectively. The bipolar coordinate system is selected for the theoretical analysis of this model, as Fig. 2 shows. The inner and outer surfaces of the annulus are thus represented by lines of constant η , which will be designated as η_i and η_o , respectively. The coordinates (ξ, η) are defined by the transformation

$$x + iy = ic \cot\left(\frac{\xi + i\eta}{2}\right) \quad (1a)$$

$$c = r_i \sinh \eta_i = r_o \sinh \eta_o \quad (1b)$$

$$\cosh \eta_i = \frac{1}{\gamma} \frac{\gamma(1 + \phi^2) + (1 - \phi^2)}{2\phi} \quad (1c)$$

$$\cosh \eta_o = \frac{\gamma(1 - \phi^2) + (1 + \phi^2)}{2\phi} \quad (1d)$$

$$\gamma = \frac{r_i}{r_o} \quad (1e)$$

$$\phi = \frac{e}{r_o - r_i} \quad (1f)$$

The liquid in the annulus is set to be Control Volume 1 (CV1). The climbing height is represented by h , and the average velocity of the meniscus is \dot{h} . The flow is assumed to be fully developed Poiseuille flow and the stress that acts on the free surface is neglected. The liquid is assumed to be isothermal during the flow process.

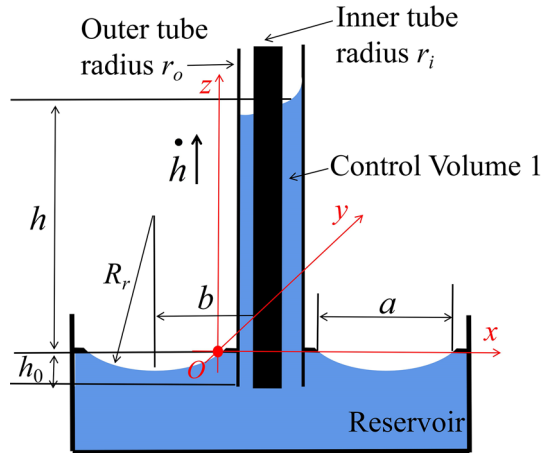


Fig. 1 Vertical cross-sectional view of capillary-driven flow in the eccentric annulus

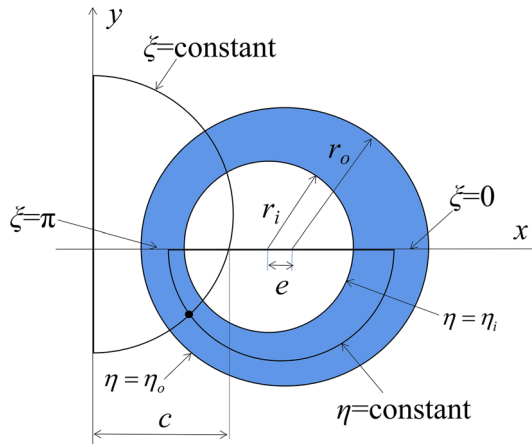


Fig. 2 Horizontal cross-sectional view of an eccentric annulus

According to reference 1, the velocity field in the z -direction u in the horizontal cross section of the annulus is

$$u(\xi, \eta, t) = -\frac{c^2}{\mu} \frac{dp}{dz} \left\{ F + E\eta - \frac{\coth \eta}{2} + \sum_{n=1}^{\infty} [A_n e^{n\eta} + (B_n - \coth \eta) e^{-n\eta}] \cos n\xi \right\} \quad (2)$$

$$F = \frac{\eta_i \coth \eta_o - \eta_o \coth \eta_i}{2(\eta_i - \eta_o)}$$

$$E = \frac{\coth \eta_i - \coth \eta_o}{2(\eta_i - \eta_o)}$$

$$A_n = \frac{\coth \eta_i - \coth \eta_o}{e^{2n\eta_i} - e^{2n\eta_o}}$$

$$B_n = \frac{e^{2n\eta_i} \coth \eta_o - e^{2n\eta_o} \coth \eta_i}{e^{2n\eta_i} - e^{2n\eta_o}}$$

where E, F, A_n and B_n are constants decided by η_i and η_o .

The boundary condition is

$$u(\xi, \eta, t)|_{\eta=\eta_i} = u(\xi, \eta, t)|_{\eta=\eta_o} = 0 \quad (3)$$

The volume flux rate across a horizontal cross section is

$$\pi(r_o^2 - r_i^2) \dot{h} = \int_{\eta_i}^{\eta_o} \int_0^{2\pi} \frac{uc^2}{(\cosh \eta - \cos \xi)^2} d\xi d\eta \quad (4)$$

From Eq. 4, the velocity field can be expressed as follows

$$u = \frac{\pi(r_o^2 - r_i^2)}{2c^2 I} \dot{h} \left\{ F + E\eta - \frac{\coth \eta}{2} + \sum_{n=1}^{\infty} [A_n e^{n\eta} + (B_n - \coth \eta) e^{-n\eta}] \cos n\xi \right\} \quad (5)$$

$$I = \int_{\eta_i}^{\eta_o} \int_0^\pi \frac{F + E\eta - \frac{\coth \eta}{2} + \sum_{n=1}^{\infty} [A_n e^{n\eta} + (B_n - \coth \eta) e^{-n\eta}] \cos n\xi}{(\cosh \eta - \cos \xi)^2} d\xi d\eta$$

The same method proposed in reference [4] is adopted here to derive the dynamic equation. The N-S equation for the z component in the Cartesian coordinate system is

$$\frac{\partial u}{\partial t} + u \frac{\partial u}{\partial z} + v \frac{\partial u}{\partial x} + w \frac{\partial u}{\partial y} = -\frac{1}{\rho} \frac{dp}{dz} + \nu \left(\frac{\partial^2 u}{\partial z^2} + \frac{\partial^2 u}{\partial x^2} + \frac{\partial^2 u}{\partial y^2} \right) + g_z \quad (6)$$

where ρ is the liquid density, ν is the kinematic viscosity, g_z is the gravity component in the z direction, v and w are velocity components in the x - and y -directions, respectively. The velocity components in x - and y -directions are both zero, and u is independent of z . In space, the magnitude of gravity is less than 10^{-4} g, as a result, for the liquid on the satellite, the *Bond* number is much smaller than 1. Therefore, g_z can be neglected. After simplification, Eq. 6 can be transformed into the bipolar coordinate system, which is written as

$$\frac{c^2}{(\cosh \eta - \cos \xi)^2} \frac{\partial u}{\partial t} + \frac{c^2}{(\cosh \eta - \cos \xi)^2} u \frac{\partial u}{\partial z} = -\frac{1}{\rho} \frac{dp}{dz} \frac{c^2}{(\cosh \eta - \cos \xi)^2} + \nu \left(\frac{\partial^2 u}{\partial \xi^2} + \frac{\partial^2 u}{\partial \eta^2} \right) \quad (7)$$

Integrating Eq. 7 with respect to η and ξ across the entire horizontal cross section of the eccentric annulus, we can obtain

$$\frac{\partial}{\partial t} \iint_{\Omega} u \frac{c^2}{(\cosh \eta - \cos \xi)^2} d\xi d\eta + \frac{c^2}{(\cosh \eta - \cos \xi)^2} \iint_{\Omega} u \frac{\partial u}{\partial z} d\xi d\eta = \dots \quad (8)$$

$$\iint_{\Omega} -\frac{1}{\rho} \frac{dp}{dz} \frac{c^2}{(\cosh \eta - \cos \xi)^2} d\xi d\eta + \iint_{\Omega} \nu \left(\frac{\partial^2 u}{\partial \xi^2} + \frac{\partial^2 u}{\partial \eta^2} \right) \frac{c^2}{(\cosh \eta - \cos \xi)^2} d\xi d\eta$$

where Ω represents the entire horizontal cross section of the eccentric annulus. Combined with Eqs. 4, 8 is integrated with respect to z from $z = -h_0$ to $z = h$, and then, the following equation is obtained.

$$\pi(r_o^2 - r_i^2) \ddot{h} = -\frac{1}{\rho} \iint_{\Omega} [p(h, t) - p(-h_0, t)] \frac{c^2}{(\cosh \eta - \cos \xi)^2} d\xi d\eta$$

$$+ \int_{-h_0}^h \iint_{\Omega} \nu \left(\frac{\partial^2 u}{\partial \xi^2} + \frac{\partial^2 u}{\partial \eta^2} \right) \frac{c^2}{(\cosh \eta - \cos \xi)^2} d\xi d\eta \quad (9)$$

The velocity distribution u is independent of z , so the second term on the left side of (9) vanishes.

The liquid–gas interface in the annulus is defined as the upper control surface of the Control Volume 1 (CV 1). The upper control surface of CV 1 is considered to be equivalent to a horizontal plane with $z = h$. The pressure on the upper control surface is

$$p(h, t) = p_0 + p_\sigma \quad (10)$$

where p_0 is the air pressure, and p_σ is the capillary pressure, which is written as

$$\pi(r_o^2 - r_i^2) p_\sigma = -2\pi\sigma(r_i \cos \alpha_i + r_o \cos \alpha_o) \quad (11)$$

When the static contact angle of liquid is 0, there exists an empirical equation for the dynamic contact angle, which is written as

$$\cos \alpha_d = 1 - 2 \tanh \left[4.96 * \left(\frac{\mu \dot{h}}{\sigma} \right)^{0.702} \right] \quad (12)$$

where μ is the dynamic viscosity of the liquid, and σ is the surface tension of liquid. This equation is presented by Jiang et al. [36], and it has been widely adopted.

With the same method adopted in reference (25), according to the geometric relationship, an approximate formula is given for calculating R_r , which is written as

$$R_r = -\frac{a^3 b}{6(r_o^2 - r_i^2)h} \tag{13}$$

According to the velocity distribution in the annulus, it can be known that $\frac{\partial u}{\partial \eta} \Big|_{\eta=\eta_i} > 0$ on the inner wall and $\frac{\partial u}{\partial \eta} \Big|_{\eta=\eta_o} < 0$ on the outer wall. Using the plus sign for the case of inner wall and the minus sign for the case of outer wall will give positive values for both cases. The friction forces on the inner and outer walls are

$$F_i = 2(h_0 + h) \int_0^\pi \mu \frac{\partial u}{\partial \eta} \Big|_{\eta=\eta_i} d\xi \tag{14a}$$

$$F_o = -2(h_0 + h) \int_0^\pi \mu \frac{\partial u}{\partial \eta} \Big|_{\eta=\eta_o} d\xi \tag{14b}$$

To calculate the pressure at the entrance of the annulus, it is necessary to build the Control Volume 2 (CV 2) around the entrance in the reservoir. The analysis is based on an equivalent circular entrance, whose radius r_e equals $\sqrt{r_o^2 - r_i^2}$, as shown in Fig. 3. In CV 2, we have

$$I_c = I_e - I_l + \Sigma F \tag{15}$$

where I_c is the rate of change of total momentum in CV 2, I_e is the flux of momentum entering CV 2, I_l is the flux of momentum leaving CV 2, and ΣF is the sum of forces acting on CV 2. The similar analysis as described in reference 24 is adopted here, and the pressure force at the entrance is obtained as below,

$$x_2 = \pi r_e^2 (p_0 + p_r) - 2\pi \mu r_e \dot{h} - \left(\frac{7}{12} + \frac{A_l}{3}\right) \pi r_e^3 \rho \ddot{h} + \frac{1}{6} \pi r_e^2 \rho \dot{h}^2 - I \tag{16}$$

$$p_r = \frac{\sigma}{R_r}$$

$$I_l = \rho \int_{\eta_i}^{\eta_o} \int_0^{2\pi} \frac{\rho u^2 c^2}{(\cosh \eta - \cos \xi)^2} d\xi d\eta$$

$$A_l = \frac{\int_{\eta_i}^{\eta_o} \int_0^{2\pi} \frac{\rho u \frac{du}{d\xi} c^2}{(\cosh \eta - \cos \xi)^2} d\xi d\eta}{\pi r_e^2 \dot{h} \ddot{h}}$$

Inserting Eqs. 10–16 into Eq. 8, the second-order differential equation for the height of the meniscus is obtained as below,

$$\ddot{h} = \frac{1}{\pi \rho r_e^2 \left[h + h_0 + \left(\frac{7}{12} + \frac{A_l}{3\rho}\right) r_e \right]} \left[\begin{aligned} & 2\pi \sigma (r_i \cos \alpha_i + r_o \cos \alpha_o) + \frac{\sigma}{R_r} \pi (r_o^2 - r_i^2) \\ & - 2\pi \mu r_e \dot{h} + \frac{1}{6} \pi r_e^2 \rho \dot{h}^2 - I_l - F_i - F_o \end{aligned} \right] \tag{17}$$

This equation can be solved using the fourth-order Runge–Kutta method with the initial conditions, $h(t = 0) = \dot{h}(t = 0) = 0$.

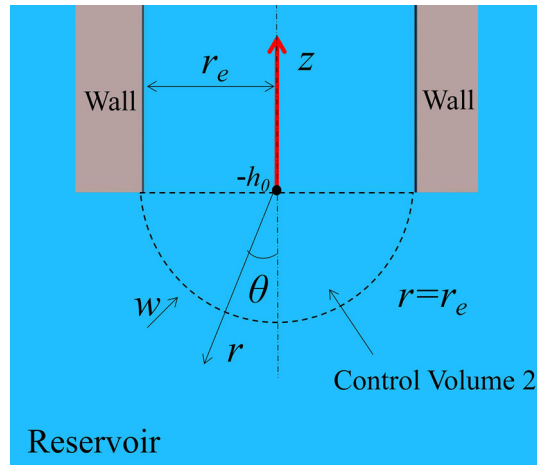


Fig. 3 An equivalent entrance and the CV 2

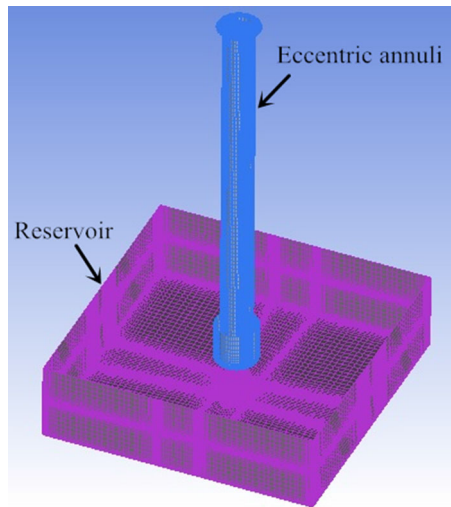


Fig. 4 3D Mesh model established for numerical simulation

3 Results and discussion

Figure 4 shows a mesh model established for numerical simulation in Fluent. Instead of a circular cylinder, a square cylinder is chosen as the reservoir for convenience. The square cylinder that has a width of 142 mm and an equivalent radius of 80 mm is used in the theoretical analysis. This simplification is acceptable because the influences of capillary pressure of the free surface in the reservoir are very small and can be neglected. The height of the model is 220 mm, and the number of grids is about 1.1 million. Boundary layers are established in the regions near all walls. The height of the first boundary layer is about 0.08 mm. The expansion ratio between two adjacent layers is 1.2.

Three kinds of silicone oil named by their kinematic viscosities (SF 1, SF 2 and SF 5) are used in the simulation. The liquid properties are shown in Table 1. The laminar flow is chosen as the flow mode in the simulation as the Re number is much smaller than 2000. Simulation parameters are listed in Table 2.

A simulation result is shown in Fig. 5a and b. In Fig. 5a, the red part represents the liquid distribution. Once the simulation begins, the liquid flows upwards quickly into the annulus. And after 2.4 s, the liquid almost reaches the top of the annulus. In Fig. 5b, the yellow surface represents the gas–liquid interface. At $t = 0$ s, all the liquid is at the bottom of the annulus. After the simulation starts, the liquid climbs upwards continuously and forms a concave surface in the annulus. Owing to the eccentricity, the free surface in the annulus is not on the same level, and it is higher on the narrow side. As shown in Fig. 6, we define $h = (h_1 + h_2 + h_3 + h_4)/4$

Table 1 Liquid properties (25°C)

Liquid	μ (kg/(m*s))	ρ (kg/m ³)	σ (N/m)	ν (10 ⁻⁶ m ² /s)
SF 1	0.000818	818	0.0169	1
SF 2	0.001746	873	0.0183	2
SF 5	0.004575	915	0.0197	5

Table 2 Numerical settings

Name	Settings
Pressure–velocity coupling equation	SIMPLEC
Spatial discretization of the pressure equation	Body force weighted
Spatial discretization of the gradient equation	Least square cell
Spatial discretization of the momentum equation	Second-order upwind scheme
Spatial discretization of the volume fraction equation	Geo-reconstruct

as the final climbing height. On the other hand, when the liquid climbs upward after the simulation starts, the liquid surface develops from a horizontal plane into an inclined curved surface. But this only occurs at the beginning of the flow. The shape of the gas–liquid interface is changing rapidly, and the duration is very short. Therefore, the effect of this process is negligible. In a fully developed capillary-driven flow, the free surface configuration almost keeps the same. The error caused by this simplification is acceptable compared to the flow distance.

Figure 7 shows the theoretical and numerical results of meniscus height vs time. The expression of velocity field contains a sum of an infinite series. To reduce calculation time and ensure accuracy at the same time, n in the expression of velocity field is set to be 3. The solid curves and square signs represent theoretical and numerical results, respectively. And the results of different liquids are plotted in different colors. Eight sizes of annuli with a wide range of eccentricity are selected. Numerical results are all in good agreement with corresponding theoretical ones.

Equation (17) can also be expressed as a sum of forces acting on CV 1, which is written as.

$$F_{ca} = F_{ia} + F_{ir} + F_{cr} + F_{fa} + F_{fr} + F_{pl} \quad (18)$$

The meanings of the force terms are:

capillary force in the annulus $F_{ca} = 2\pi(r_i \cos \alpha_i + r_o \cos \alpha_o)\sigma$.

inertia force in the reservoir $F_{ir} = \rho\pi r_e^2 \left[\left(\frac{7}{12} + \frac{A_l}{3\rho} \right) r_e + h_0 \right] \ddot{h}$.

pressure loss force at the entrance $F_{pl} = I_l - \frac{1}{6}\rho\pi r_e^2 \dot{h}^2$.

friction force in the annulus $F_{fa} = F_i + F_o$.

capillary force in the reservoir $F_{cr} = \frac{6\pi r_e^4}{a^3 b} \sigma h$.

friction force in the reservoir $F_{fr} = 2\pi\mu r_e \dot{h}$.

inertia force in the annulus $F_{ia} = \rho\pi r_e^2 h \ddot{h}$.

The development of different forces vs time is shown in Fig. 8. The liquid is SF 1, with $r_i = 3$ mm, $r_o = 6$ mm, $e = 0.8$ mm, and $h_0 = 15$ mm. The capillary force in the annulus always plays a dominant role. The inertia force in the reservoir has a maximum value at the beginning and decreases rapidly. The pressure loss force at the entrance increases with time until it reaches the maximum value and then decreases with time thereafter. The friction force in the annulus increases with time, and finally, it will be close to the capillary force in the annulus. In a flow for a long period of time, it can be considered that the flow is governed by the friction force and the capillary force in the annulus. While in the beginning of a capillary flow, the inertia force in the reservoir and the pressure loss force at the entrance should also be considered; otherwise, the theoretical results will have unacceptable deviations. In some previous study of capillary-driven flows [9], the pressure loss at the entrance is neglected and the deviation between theoretical and experimental results in the beginning of flow is unacceptable. The capillary force in the reservoir is too small to identify under this condition.

The liquid flow speed increases as the eccentricity increases due to the decrease of the friction force in the annulus. For example, as shown in Fig. 7a, after 2.4 s, the theoretical flow distance of SF 1 is 142.7 mm, while

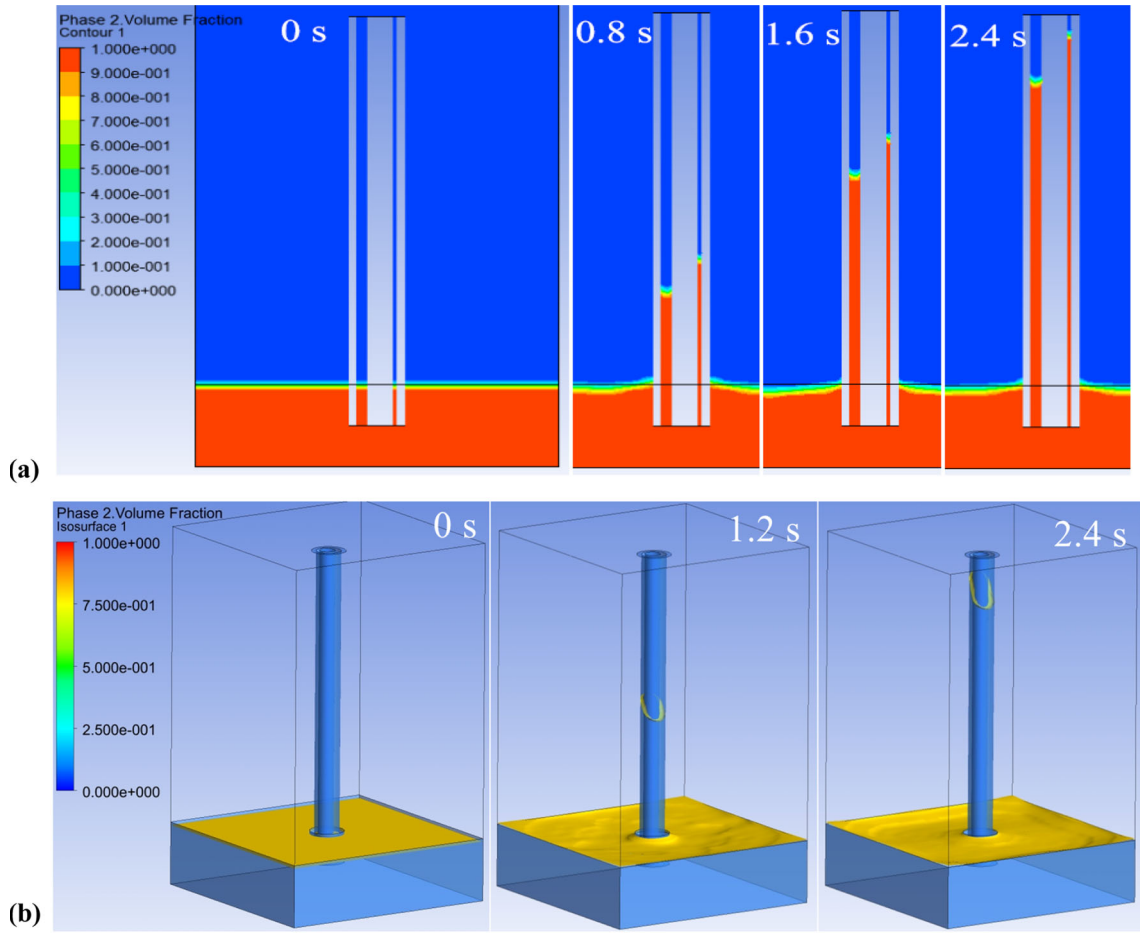


Fig. 5 A numerical result of capillary-driven flow with the liquid of SF 1 and $r_i = 5$ mm, $r_o = 8$ mm, $e = 1.5$ mm and $h_0 = 15$ mm. **a** Liquid distribution in the vertical cross section of the annulus. **b** Height of free surface vs time

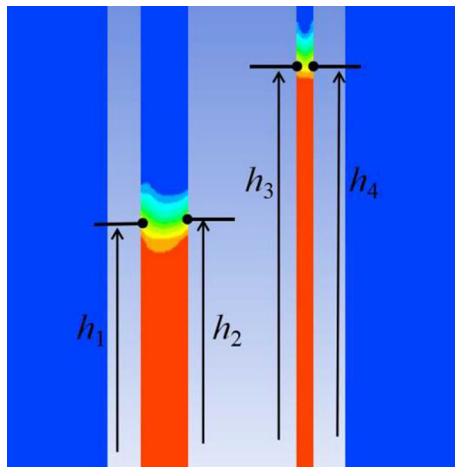


Fig. 6 Meniscus height at different positions

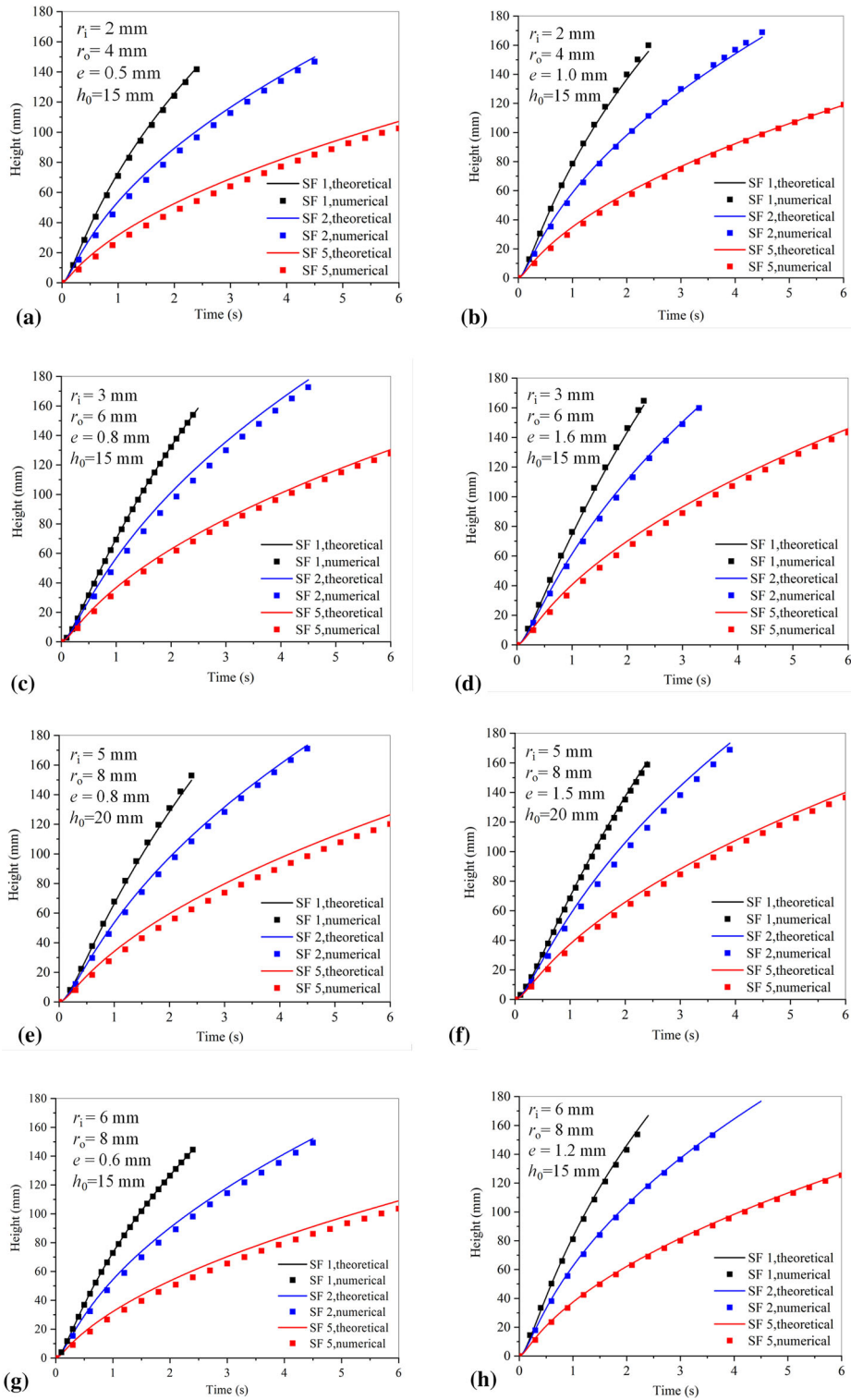


Fig. 7 Comparison between theoretical and numerical results. **a** $r_i = 2$ mm, $r_o = 4$ mm, $e = 0.5$ mm, $h_0 = 15$ mm, **b** $r_i = 2$ mm, $r_o = 4$ mm, $e = 1.0$ mm, $h_0 = 15$ mm, **c** $r_i = 3$ mm, $r_o = 6$ mm, $e = 0.8$ mm, $h_0 = 15$ mm, **d** $r_i = 3$ mm, $r_o = 6$ mm, $e = 1.6$ mm, $h_0 = 15$ mm, **e** $r_i = 5$ mm, $r_o = 8$ mm, $e = 0.8$ mm, $h_0 = 20$ mm, **f** $r_i = 5$ mm, $r_o = 8$ mm, $e = 1.5$ mm, $h_0 = 20$ mm, **g** $r_i = 6$ mm, $r_o = 8$ mm, $e = 0.6$ mm, $h_0 = 15$ mm, **h** $r_i = 6$ mm, $r_o = 8$ mm, $e = 1.2$ mm, $h_0 = 15$ mm

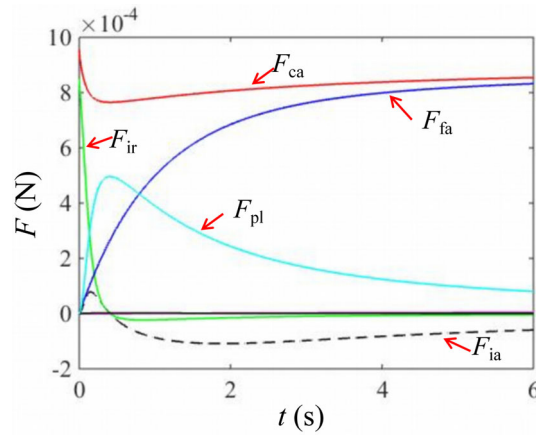


Fig. 8 Development of forces vs time for SF 1, $r_i = 3$ mm, $r_o = 6$ mm, $e = 0.8$ mm, and $h_0 = 15$ mm

Table 3 Numerical parameters

No	r_i (mm)	r_o (mm)	E (mm)	h_0 (mm)	Liquid	v_{\max} (mm/s)	Re_{\max}
#1	2	4	0.5	15	SF 1	87.2	302
#2	2	4	0.5	15	SF 2	68.6	119
#3	2	4	0.5	15	SF 5	42.1	29.2
#4	2	4	1.0	15	SF 1	91.5	317
#5	2	4	1.0	15	SF 2	73.1	127
#6	2	4	1.0	15	SF 5	46.1	31.9
#7	3	6	0.8	15	SF 1	79.4	413
#8	3	6	0.8	15	SF 2	66.3	172
#9	3	6	0.8	15	SF 5	45.2	47.0
#10	3	6	1.6	15	SF 1	84.3	438
#11	3	6	1.6	15	SF 2	71.0	184
#12	3	6	1.6	15	SF 5	49.2	51.1
#13	5	8	0.8	20	SF 1	76.3	476
#14	5	8	0.8	20	SF 2	62.4	195
#15	5	8	0.8	20	SF 5	41.0	51.2
#16	5	8	1.5	20	SF 1	80.1	500
#17	5	8	1.5	20	SF 2	66.3	207
#18	5	8	1.5	20	SF 5	44.5	55.6
#19	6	8	0.6	15	SF 1	86.7	459
#20	6	8	0.6	15	SF 2	68.5	181
#21	6	8	0.6	15	SF 5	42.4	44.9
#22	6	8	1.2	15	SF 1	96.6	511
#23	6	8	1.2	15	SF 2	77.1	204
#24	6	8	1.2	15	SF 5	48.8	51.6

in Fig. 7b, it is 155.7 mm. The maximum flow speed of liquid also increases as the eccentricity increases. As shown in Table 3, in the annulus with $r_i = 3$ mm and $r_o = 6$ mm, when $e = 0.8$ mm, the maximum speed is 66.3 mm/s for SF 2, while it is 71.0 mm/s when $e = 1.6$ mm. The development of the friction force in the annulus is shown in Fig. 9a and b. Figure 9a shows the results of SF 1, and Fig. 9b shows the results of SF 5. The black curves represent the results of the case with $r_i = 5$ mm and $r_o = 8$ mm. The blue curves represent the results of the case with $r_i = 3$ mm and $r_o = 6$ mm. The red curves represent the results of the case with $r_i = 2$ mm and $r_o = 4$ mm. And the values of eccentricity are labeled in the lower right corners of the figures. It can be seen that, for different liquids or annuli with different values of γ , the increase in eccentricity will lead to the decrease of the friction force in the annulus, which leads to the increase in liquid flow speed. Besides, the longer the flow distance of the liquid, the smaller the difference between the friction forces in different annuli.

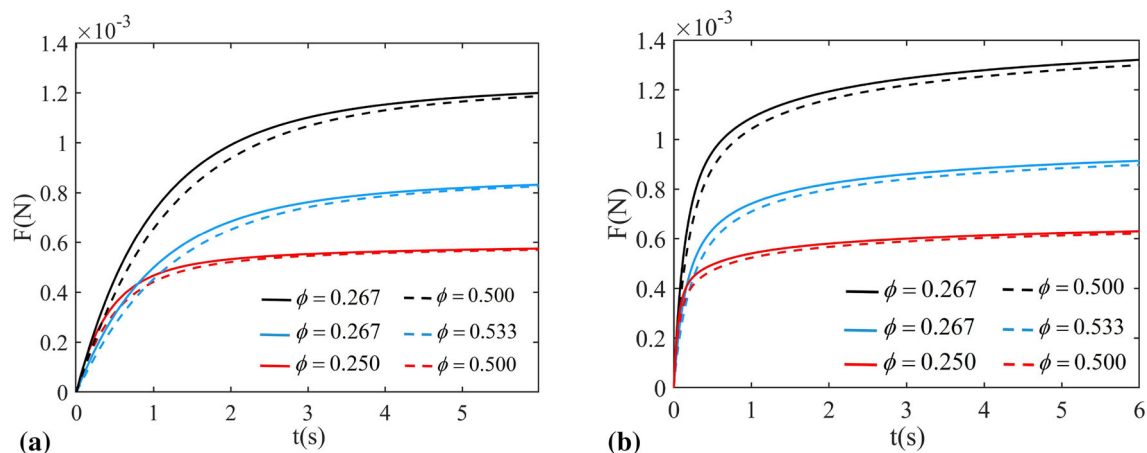


Fig. 9 Development of friction forces vs time. The black curves represent the case $r_i = 5$ mm $r_o = 8$ mm; the blue curves represent the case $r_i = 3$ mm, $r_o = 6$ mm; the red curves represent the case $r_i = 2$ mm, $r_o = 4$ mm. **a** Liquid SF 1. **b** Liquid SF 5

4 Conclusions

An exact differential equation for capillary-driven flow in an eccentric annulus under microgravity is proposed for the first time and verified by numerical simulation. Eight sizes of eccentric annuli and three types of silicone oil are adopted. The theoretical results are in good agreement with numerical results. Capillary-driven flows in eccentric annuli under microgravity can be predicted accurately with this equation.

The development of different forces is analyzed comprehensively, and different flow features are obtained. Besides, the effects of eccentricity on flow resistance and flow speed are discussed. The flow resistance in the annulus decreases with the increase in eccentricity, which leads to the increase in flow speed.

This can deepen people's understanding and fill the gap in the knowledge of capillary-driven flow. The conclusions proposed in this paper will be helpful for liquid management under microgravity, especially for the design of tube bundles.

Acknowledgements We are really grateful for Prof. Li Duan. She offered many suggestions when preparing the manuscript in the beginning. This study was funded by the China Manned Space Engineering Program (Fluid Physics Experimental Rack and the Priority Research Program of Space Station), and the Natural Science Foundation Project (No. 12032020).

Data availability The data of this paper can be obtained by contacting the corresponding author.

Declarations

Conflict of interest The authors declare no competing financial interest.

References

1. Snyder, W.T., Goldstein, G.A.: An analysis of fully developed laminar flow in an eccentric annulus. *AICHE J* **11**(3), 462–467 (1965). <https://doi.org/10.1002/aic.690110319>
2. Washburn, E.W.: The dynamics of capillary flow. *Phys. Rev.* **17**, 273–283 (1921)
3. Levine, S., Reed, P., Watson, E.J., Neale, G.: A theory of the rate of rise of a liquid in a capillary. *Colloid and Interface Sci.* **3**, 403–419 (1976). <https://doi.org/10.1016/b978-0-12-404503-3.50048-3>
4. Stange, M., Dreyer, M., Rath, H.J.: Capillary driven flow in circular cylindrical tubes. *Phys. Fluids* **15**, 2587–2601 (2003). <https://doi.org/10.1063/1.1596913>
5. Chen, S.T., Ye, Z.J., Duan, L., Kang, Q.: Capillary driven flow in oval tubes under microgravity. *Phys. Fluids* **33**(3), 032111 (2021). <https://doi.org/10.1063/5.0040993>
6. Tsori, Y.: Discontinuous liquid rise in capillaries with varying cross-sections. *Langmuir* **22**, 8860–8863 (2006). <https://doi.org/10.1021/la061605x>

7. Liou, W.W., Peng, Y.Q., Parker, P.E.: Analytical modeling of capillary flow in tubes of nonuniform cross section. *J. Colloid Interface Sci.* **333**, 389–399 (2009). <https://doi.org/10.1016/j.jcis.2009.01.038>
8. Cheng, X., Chen, Y., Li, H.R., Li, B.X., Han, X., Xin, G.M.: Investigation on capillary flow in tubes with variable diameters. *J. Porous Media* **22**(13), 1627–1638 (2019). <https://doi.org/10.1615/jpormedia.2019026774>
9. Lei, J., Xu, Z., Xin, F., Lu, T.J.: Dynamics of capillary flow in an undulated tube. *Phys. Fluids* **33**(5), 05210, 9 (2021). <https://doi.org/10.1063/5.0048868>
10. Lei, J.C., Sun, H., Liu, S.B., Feng, S.S., Lu, T.J.: Hypergravity effect on dynamic capillary flow in inclined conical tubes with undulated inner walls. *Microgravity Sci. Technol.* **34**, 71 (2022). <https://doi.org/10.1007/s12217-022-09996-7>
11. Daniel, A.B., Chen, Y.K., Semerjian, B., Tavan, N., Weislogel, M.M.: Compound capillary flows in complex containers: drop tower test results. *Microgravity Sci. Technol.* **22**, 475–485 (2010). <https://doi.org/10.1007/s12217-010-9213-x>
12. Chassagne, R., Dörfler, F., Guyenot, M., Harting, J.: Modeling of capillary-driven flows in axisymmetric geometries. *Comput. Fluids* **178**, 132–140 (2019). <https://doi.org/10.1016/j.compfluid.2018.08.024>
13. Sufia, K., Jyoti, P., Singh, B.S.: An analytical solution of the inverse problem of capillary imbibition. *Phys. Fluids* **32**(4), 041704 (2020). <https://doi.org/10.1063/5.0008081>
14. Wang, Q.G., Li, L., Gu, J.P., Weng, N.: A dynamic model for the oscillatory regime of liquid rise in capillaries. *Chem. Eng. Sci.* **209**, 115220 (2019). <https://doi.org/10.1016/j.ces.2019.115220>
15. Wang, C.X., Xu, S.H., Sun, Z.W., Hu, W.R.: Influence of contact angle and tube size on capillary-driven flow under microgravity. *AIAA J.* **47**(11), 2642 (2009). <https://doi.org/10.2514/1.41899>
16. Wang, C.X., Xu, S.H., Sun, Z.W., Hu, W.R.: A study of the influence of initial liquid volume on the capillary in interior corner under microgravity. *Int. J. Heat Mass Tran.* **53**(9–10), 1801 (2010). <https://doi.org/10.1016/j.ijheatmasstransfer.2010.01.009>
17. Weislogel, M.M., Lichter, S.: Capillary flow in an interior corner. *J. Fluid Mech.* **373**, 349–378 (1998). <https://doi.org/10.1017/s0022112098002535>
18. Weislogel, M.M., Nardin, C.L.: Capillary driven flow along interior corners formed by planar walls of varying wettability. *Microgravity Sci. Technol.* **17**(3), 45–55 (2005). <https://doi.org/10.1007/BF02872087>
19. Chen, Y.K., Weislogel, M.M., Nardin, C.L.: Capillary driven flows along rounded interior corners. *J. Fluid Mech.* **556**, 235–271 (2006). <https://doi.org/10.1007/bf02872087>
20. Li, Y.Q., Hu, M.Z., Liu, L., Su, Y.Y., Duan, L., Kang, Q.: Study of capillary driven flow in an interior corner of rounded wall under microgravity. *Microgravity Sci. Technol.* **27**, 193–205 (2015). <https://doi.org/10.1007/s12217-015-9435-z>
21. Higuera, F.J., Medina, A., Linan, A.: Capillary rise of a liquid between two vertical plates making a small angle. *Phys. Fluids* **20**, 102102 (2008). <https://doi.org/10.1063/1.3000425>
22. Wu, Z.Y., Huang, Y.Y., Chen, X.Q., Zhang, X.: Capillary driven flows along curved interior corners. *Int. J. Multiphase Flow* **109**, 14–25 (2018). <https://doi.org/10.1016/j.ijmultiphaseflow.2018.04.00>
23. Tian, Y., Jiang, Y., Zhou, J.J., Doi, M.: Dynamics of Taylor rising. *Langmuir* **35**, 5183–5190 (2019). <https://doi.org/10.1021/acs.langmuir.9b00335>
24. Zhou, J.J., Doi, M.: Universality of capillary rising in corners. *J. Fluid Mech.* **900**, A29 (2020). <https://doi.org/10.1017/jfm.2020.531>
25. Dreyer, M., Delgado, A., Rath, H.J.: Capillary rise of liquid between parallel plates under microgravity. *J. Colloid Interface Sci.* **163**, 158–168 (1994). <https://doi.org/10.1006/jcis.1994.1092>
26. Wolf, F., Santos, L., Phillippi, P.: Capillary rise between plates under dynamic conditions. *J. Colloid Interface Sci.* **344**, 171–179 (2010). <https://doi.org/10.1016/j.jcis.2009.12.023>
27. Weng, N., Wang, Q.G., Li, J.D., Lyu, J.F., Zhang, H.X., Yao, W.: Liquid penetration in metal wire mesh between parallel plates under normal gravity and microgravity conditions. *Appl. Therm. Eng.* **167**, 114722 (2019). <https://doi.org/10.1016/j.applthermaleng.2019.114722>
28. Klatte, J., Haake, D., Weislogel, M.M., Dreyer, M.: A fast numerical procedure for steady capillary flow in open channels. *Acta Mech.* **201**, 269–276 (2008). <https://doi.org/10.1007/s00707-008-0063-1>
29. Bauer, F.: Axial response of differently excited anchored viscous liquid bridges in zero-gravity. *Arch. Appl. Mech.* **63**(4–5), 322–336 (1993). <https://doi.org/10.1007/bf00793898>
30. Schilling, U., Siekmann, J.: Numerical study of equilibrium capillary surfaces under low gravitational conditions. *Arch. Appl. Mech.* **60**(3), 176–182 (1990). <https://doi.org/10.1007/bf00539587>
31. Aksel, N.: Influence of the capillarity on a creeping film flow down an inclined plane with an edge. *Arch. Appl. Mech.* **70**(1–3), 81–90 (2000). <https://doi.org/10.1007/s004199900039>
32. Chen, S.T., Duan, L., Kang, Q.: Study on propellant management device in plate surface tension tanks. *Acta Mech. Sinica* **37**(10), 1501–1511 (2021). <https://doi.org/10.1007/s10409-021-01121-y>
33. Wang, L., Zhang, X., Yun, Y., Liu, J., Li, W., Huang, B.: Numerical simulation of the reorientation process under different conditions in a vane-type surface tension propellant tank. *Microgravity Sci. Technol.* **34**, 37 (2022). <https://doi.org/10.1007/s12217-022-09950-7>
34. Zhang, D., Meng, L.: Numerical simulation analysis of liquid transportation in capsule-type vane tank under microgravity. *Microgravity Sci. Technol.* **32**, 817–824 (2020). <https://doi.org/10.1007/s12217-020-09811-1>
35. Li, J., Lin, H., Li, K., Zhao, J., Hu, W.: Liquid sloshing in partially filled capsule storage tank undergoing gravity reduction to low/micro-gravity condition. *Microgravity Sci. Technol.* **32**, 587–596 (2020). <https://doi.org/10.1007/s12217-020-09801-3>
36. Jiang, T.S., Oh, S.G., Slattery, J.C.: Correlation for dynamic contact angle. *J. Colloid Interface Sci.* **69**, 74–77 (1979). [https://doi.org/10.1016/0021-9797\(79\)90081-x](https://doi.org/10.1016/0021-9797(79)90081-x)

Publisher's Note Springer Nature remains neutral with regard to jurisdictional claims in published maps and institutional affiliations.

Springer Nature or its licensor (e.g. a society or other partner) holds exclusive rights to this article under a publishing agreement with the author(s) or other rightsholder(s); author self-archiving of the accepted manuscript version of this article is solely governed by the terms of such publishing agreement and applicable law.